



# Unraveling reactive oxygen species-dependent toluene mineralization routes via construction of $\text{Ti}_x\text{Sn}_{1-x}\text{O}_2$ infinite solid solution photocatalysts

Qi Li<sup>a</sup>, Zi-han Yue<sup>a</sup>, Mi-sha Shan<sup>a</sup>, Yi-lei Li<sup>a,b</sup>, Ying Liu<sup>a</sup>, Ying-juan Hao<sup>a</sup>, Fa-tang Li<sup>a,\*</sup>

<sup>a</sup> Hebei Key Laboratory of Photoelectric Control on Surface and Interface, College of Science, Hebei University of Science and Technology, Shijiazhuang 050018, China

<sup>b</sup> Key Laboratory of Theoretical and Computational Photochemistry, Ministry of Education, College of Chemistry, Beijing Normal University, Beijing 100875, China

## ARTICLE INFO

### Keywords:

Photocatalysis

$\text{SnO}_2$

Toluene

Intermediates

Infinite solid solution

## ABSTRACT

Intermediates seriously affect the reaction process and rate in terms of kinetics. However, there are few studies on the effect of reactive oxygen species on intermediates of toluene mineralization. Herein,  $\text{SnO}_2$  and  $\text{Ti}_x\text{Sn}_{1-x}\text{O}_2$  infinite solid solution photocatalysts are prepared and the mineralization ability of  $\text{Ti}_{0.1}\text{Sn}_{0.9}\text{O}_2$  is 2.7 times that of  $\text{SnO}_2$ . Introduction of Ti shifts the conduction band position upward, providing thermodynamic possibility for superoxide radicals formation. The sole hydroxyl radicals over  $\text{SnO}_2$  lead to the generation of benzyl alcohol; while synergetic hydroxyl radicals and superoxide radicals result in benzoic acid existed in solid solution catalysts. Theoretical calculation confirms that benzoic acid has lower ring opening barrier, thereby improving toluene mineralization ability over  $\text{Ti}_x\text{Sn}_{1-x}\text{O}_2$ . The synergetic roles of Ti and Sn in adsorption and activation of water and toluene molecules are also proposed. This work provides new insights into reactive oxygen radicals regulation to alter intermediates and ease toluene removal.

## 1. Introduction

As a volatile organic compound with serious harm to human, toluene has attracted extensive attention of researchers [1]. Photocatalytic technology has great application potential in the degradation of toluene due to its mild, economical and green characteristics [2]. In the photocatalytic degradation of toluene, the differences in the ring-opening reactions of different intermediates directly affect the efficiency of degradation [3]. Therefore, the selectivity of photocatalyst for intermediates is an important factor affecting the photocatalytic performance. However, the selective mechanism of photocatalyst for toluene intermediates has been seldom explored.

The key problem of photocatalytic degradation of toluene is the poor degradation performance. Generally, the oxidation ability of photocatalysts is closely related to the valence band position [4]. In order to effectively remove toluene, many photocatalytic materials have been tried. For example, oxides including  $\text{ZnO}$  [5],  $\text{TiO}_2$  [6],  $\text{WO}_3$  [7] and bismuth-based materials such as  $\text{BiOX}$  ( $X = \text{Cl}, \text{Br}$ ) [8,9],  $\text{BiVO}_4$  [10] etc. Among them, a study showed that the degradation yield of toluene under  $\text{BiOCl}$  reached only about 40% in closed circulation system within 60 min [11]. Although  $\text{ZnO}$  and  $\text{WO}_3$  have superior photocatalytic degradation performance of toluene than  $\text{BiOCl}$  in closed system [12],

their performance in flow system still needs to be improved.  $\text{TiO}_2$  has high photocatalytic activity. However, the characteristic of easy deactivation is a fatal defect that limits its application [13]. Therefore, it is urgent to seek catalysts with high degradation activity and good stability in the flow system to meet the needs of industrialization.  $\text{SnO}_2$  is an attractive candidate for photocatalytic degradation of toluene due to its strong oxidation performance, which is attributed to the low valence band position [14]. Therefore, Sn is chosen as the major metal element.

The construction of solid solution is considered to be an effective method to further improve photocatalytic performance because it can not only enhance the utilization of visible light, but also effectively improve the separation of photogenerated electron-hole pairs [15]. It is fascinating to introduce Ti ions into  $\text{SnO}_2$  photocatalyst to construct  $\text{Ti}_x\text{Sn}_{1-x}\text{O}_2$  solid solution. On the one hand, Ti ions have the same valence state and coordination mode as Sn ions, which makes the solid solution easier to prepare due to easier control of equivalence substitution and wider substitution range. On the other hand, the ionic radius of Ti (0.061 nm) is slightly smaller than that of Sn (0.069 nm), which leads to stronger atomic connections within the formed solid solution and thus enhances the photo-stability of the catalyst [16]. Therefore, it is of practical significance to prepare  $\text{Ti}_x\text{Sn}_{1-x}\text{O}_2$  photocatalysts to study their performance in photocatalytic degradation of toluene.

\* Corresponding author.

E-mail address: [lifatang@hebust.edu.cn](mailto:lifatang@hebust.edu.cn) (F.-t. Li).

<https://doi.org/10.1016/j.apcatb.2023.122628>

Received 1 January 2023; Received in revised form 2 March 2023; Accepted 12 March 2023

Available online 13 March 2023

0926-3373/© 2023 Elsevier B.V. All rights reserved.

In photocatalytic reactions, reactive oxygen species generated by the activation of molecular oxygen play a critical role. Due to strong oxidizing properties, they can not only attack the active site of target compound to destroy its original structure [17], but also attack a specific atom leading to selective oxidation reactions or cross-coupling reactions [18] etc. However, how reactive oxygen species affect the formation of intermediates of organic pollutants such as toluene has rarely been studied, and the difference in toluene degradation reaction path caused by different reactive oxygen species generated by  $\text{SnO}_2$  and its solid solution has not been reported.

Our group has recently found that hydroxyl radicals can lead to the formation of phenolic intermediates, which have reverse inhibitory effect on the ring-opening reaction of toluene and would cover the active sites, resulting in the inactivation of photocatalysts [19]. Then whether the existence of superoxide radicals affects the mineralization of toluene needs to be further investigated. Herein,  $\text{SnO}_2$  and  $\text{Ti}_x\text{Sn}_{1-x}\text{O}_2$  were prepared for photocatalytic degradation of toluene due to the introduction of Ti will cause the difference of superoxide radicals related to energy band structure, and the toluene degradation mechanism was investigated using in situ diffuse reflectance infrared fourier transform (in-situ DRIFT) spectroscopy and DFT calculations. The degradation yield of toluene was significantly enhanced in the presence of  $\text{Ti}_x\text{Sn}_{1-x}\text{O}_2$  compared to pure  $\text{SnO}_2$  due to the synergistic effect of Sn and Ti sites. In addition, the selectivity of different photocatalysts for the intermediates of toluene was revealed and the different toluene degradation pathways caused by the difference of reactive oxygen species in  $\text{SnO}_2$  and  $\text{Ti}_x\text{Sn}_{1-x}\text{O}_2$  were clarified. In conclusion, this work provides new insights for the reactive oxygen radical regulation to change reaction path, and provides a reference for photocatalysts design.

## 2. Experimental

### 2.1. Chemicals

Tin tetrachloride pentahydrate ( $\text{SnCl}_4 \cdot 5 \text{H}_2\text{O}$ ), tetrabutyl titanate ( $\text{C}_{16}\text{H}_{36}\text{O}_4\text{Ti}$ ), ethanol ( $\text{C}_2\text{H}_5\text{OH}$ ), sodium hydroxide ( $\text{NaOH}$ ), all are AR grade and have not been further purified.

### 2.2. Photocatalysts preparation

#### 2.2.1. The preparation of $\text{SnO}_2$

In typical preparation process [20], 1 mmol  $\text{SnCl}_4 \cdot 5 \text{H}_2\text{O}$  was first dissolved in 10 mL deionized water to form  $\text{SnCl}_4$  solution. Subsequently, 10 mL of 1 mmol  $\text{NaOH}$  solution was dropped into the  $\text{SnCl}_4$  solution and stirred for 15 min to make it become  $\text{SnOH}$  precursor. Later, 10 mL ethanol was added to the above solution and stirred continuously for 10 min to make the solution mixed evenly. Finally, the solution was transferred to 50 mL polytetrafluoro reactor and reacted in an oven at  $180^\circ\text{C}$  for 720 min. The obtained sample was washed with water and ethanol for three times to remove the residual ions and dried in an oven at  $70^\circ\text{C}$ . Finally, the obtained pure  $\text{SnO}_2$  photocatalyst was used for the subsequent photocatalytic degradation of toluene.

#### 2.2.2. The preparation of $\text{Ti}_x\text{Sn}_{1-x}\text{O}_2$

Different  $\text{Ti}_x\text{Sn}_{1-x}\text{O}_2$  photocatalysts were prepared by adjusting the ratio of  $\text{SnCl}_4 \cdot 5 \text{H}_2\text{O}$  to  $\text{C}_{16}\text{H}_{36}\text{O}_4\text{Ti}$  and maintaining the total amount at 5 mmol [21]. Taking  $\text{Ti}_{0.1}\text{Sn}_{0.9}\text{O}_2$  as an example, 4.5 mmol  $\text{SnCl}_4 \cdot 5 \text{H}_2\text{O}$  was dissolved in 35 mL ethanol and stirred continuously for 10 min to make the concentration uniform. Then 0.5 mmol  $\text{C}_{16}\text{H}_{36}\text{O}_4\text{Ti}$  was added and stirred for another 15 min to disperse evenly. After that, the solution was transferred to 50 mL polytetrafluoro reactor and the reaction was carried out in an oven at  $180^\circ\text{C}$  for 720 min. After cooling to room temperature, the obtained photocatalyst was collected and washed with water and ethanol for three times, and maintained in an oven at  $70^\circ\text{C}$  for 720 min to obtain pure and dry  $\text{Ti}_x\text{Sn}_{1-x}\text{O}_2$  photocatalyst.

### 2.3. Characterization

X-ray diffractometer (Rigaku D/MAX 2500) is used for X-ray diffraction (XRD) of the type and crystal phase of catalyst. Field emission scanning electron microscope (FE-SEM, HITACHI SU8010) and JEM-2100 F transmission electron microscope (TEM) were used to observe the micromorphology and element distribution of samples. The surface composition and element content of catalysts were determined by X-ray photoelectron spectroscopy (XPS) analysis on Thermo Fisher Scientific K-Alpha spectrometer with Al K alpha source. The adsorb oxygen ability of photocatalyst was measured by  $\text{O}_2$  temperature programmed destruction ( $\text{O}_2$ -TPD) test on the chemical adsorption instrument (PC-1200). Photoluminescence (PL) spectra were presented on fluorescence spectrophotometer (Hitachi F-4600) to analyze the charge separation efficiency of photocatalysts. JEOL JES-FA300 electron paramagnetic resonance spectrometry was used for EPR spin capture test to analyze reactive oxygen species generated in reaction system. Hitachi U-4100 UV-Vis diffuse reflectance spectrometer was used to measure UV-Vis diffuse reflectance spectrum (DRS) to judge the light absorption and band gap energy of samples. Mott-Schottky test was performed on CHI-660E electrochemical workstation to analyze the energy band structure of catalysts.

### 2.4. The photocatalytic degradation of toluene

The degradation performance of prepared photocatalyst was measured in flow reaction system at room temperature. As shown in Fig. S1, the feed gas consisted of three gas paths including dry synthetic air, wet synthetic air and toluene in nitrogen. The initial concentration of toluene was maintained at 120 ppm by controlling the flow rate of synthetic air and  $\text{N}_2$  are 95 mL/min and 9 mL/min, respectively, and maintaining the temperature of bubbler containing toluene liquid at  $-2^\circ\text{C}$  by connecting with constant temperature circulating water bath. The feed gas was mixed in the mixing tank and then flowed into the reactor, where 0.5 g uniformly dispersed photocatalyst was placed. In addition, two 300 W xenon lamps were placed about 35 cm above the reactor for the photocatalytic degradation of toluene. The flowing gas flowed out of the reactor and then was analyzed by gas chromatography (GC-7920) for composition and content. Finally, the concentration of toluene and the generated  $\text{CO}_2$  at any time can be obtained through gas chromatography detector.

The degradation efficiency of toluene can be obtained by the following equation :

$$D = \frac{[\text{C}_7\text{H}_8]_{\text{Initial}} - [\text{C}_7\text{H}_8]_{\text{out}}}{[\text{C}_7\text{H}_8]_{\text{Initial}}} * 100\%$$

The mineralization yield of toluene can be obtained by the following equation :

$$M = \frac{[\text{CO}_2]}{[\text{C}_7\text{H}_8]_{\text{Initial}} * 7} * 100\%$$

where  $[\text{C}_7\text{H}_8]_{\text{Initial}}$  represents the initial concentration of toluene,  $[\text{C}_7\text{H}_8]_{\text{out}}$  indicates the concentration of toluene after reaction, and  $[\text{CO}_2]$  represents the concentration of  $\text{CO}_2$  generated. All units are ppm.

### 2.5. EPR test

EPR test was carried out on electronic paramagnetic resonance instrument (JES-FA300, Japan). Firstly, 5 mg sample was dispersed in 10 mL deionized water by ultrasonic treatment at room temperature. Later, 200  $\mu\text{L}$  DMPO solution with a concentration of 50 mM was added to 200  $\mu\text{L}$  dispersion. After the solution was mixed evenly, the tests were carried out under dark and illumination conditions, respectively.

## 2.6. In situ DRIFT test

In the in situ infrared device (Bruker Invenio S), in situ diffuse reflection cell, xenon lamp and infrared spectrometer were equipped. Similar to the photocatalytic toluene degradation reaction system, DRIFT system is also a flow system and the feed gas is formed by mixing dry air, wet air, and toluene gas (in  $N_2$ ) (Fig. S2). Since the most important parameter in toluene degradation reaction is the toluene initial concentration before entering the reactor, the toluene concentration in situ DRIFT is set to be consistent with the performance test by adjusting the gas path and flow rate. Specifically, the initial concentration of toluene is maintained at about 120 ppm by controlling the flow rate of toluene standard gas stream with 350 ppm concentration and two air streams at 50 mL/min. Subsequently, the mixed feed gas was injected into the in situ diffuse reflection cell with photocatalyst. The photocatalyst was adsorbed under dark condition for about 20 min to reach adsorption-desorption equilibrium, and adsorption signals were collected every two minutes to monitor the intermediate species under dark condition. Afterwards, xenon lamp equipped with optical fiber was illuminated at the light passages of in situ diffuse reflection cell to simulate the reaction environment of photocatalytic degradation of toluene. Infrared spectral signals were collected every 2 min and maintained for 30 min to monitor the reaction intermediates during illumination process. Finally, the obtained DRIFT spectra in the range of 1000–4000  $cm^{-1}$  were analyzed to investigate the mechanism of photocatalytic degradation of toluene.

## 2.7. DFT analysis

All the calculations are implemented by the VASP code [22]. The

Generalized Gradient Approximation (GGA)-Perdew Burke Ernzerhof (PBE) functional is selected for the exchange and correlation potential [23]. Weak van der Waals interaction is considered by the DFT-D<sub>3</sub> functional [24]. The cut off energy for the plane-wave is 400 eV. A  $2 \times 2 \times 1$  k-mesh in the Brillouin-zone is chosen for integration. Total energies of the systems converge to  $10^{-5}$  eV in the iteration solution of Kohn-Sham equation. The force on each atoms reduce to 0.05 eV/Å after geometry optimization. A vacuum layer of more than 15 Å is added vertical to the surface  $SnO_2$ .

## 3. Results and discussion

### 3.1. Structure and morphology

The XRD patterns (Fig. 1a) demonstrate that the prepared  $SnO_2$  is tetragonal crystalline phase (JCPDS NO. 41–1445). With the increase of the amount of Ti, the diffraction peaks of samples shift to the large angle direction, implying a smaller lattice parameters [25]. This is attributed to the small ionic radius of Ti ions, suggesting the successful introduction of Ti ions into the lattice of  $SnO_2$ . Notably, when the content of Ti cations reaches 50%, the  $TiO_2$  crystalline phase is still not detected, indicating that  $SnO_2$  and  $TiO_2$  form infinite solid solution, and the crystal structure diagram is shown in Fig. 1b.

In TEM image shown in Fig. 1c, there are lattice fringes with lattice spacing of 0.333 nm in prepared  $SnO_2$ , corresponding to the (110) facet of tetragonal crystalline phase  $SnO_2$  (theoretical value is 0.335 nm). In  $Ti_{0.1}Sn_{0.9}O_2$ , the lattice fringes with lattice spacing of 0.334 nm corresponding to the  $SnO_2$  (110) facet could be observed (Fig. 1d). Due to the amount of Ti ions in  $Ti_{0.1}Sn_{0.9}O_2$  is low, it is difficult to judge the effect of displacement on lattice spacing, so the HRTEM test of  $Ti_{0.5}Sn_{0.5}O_2$  is

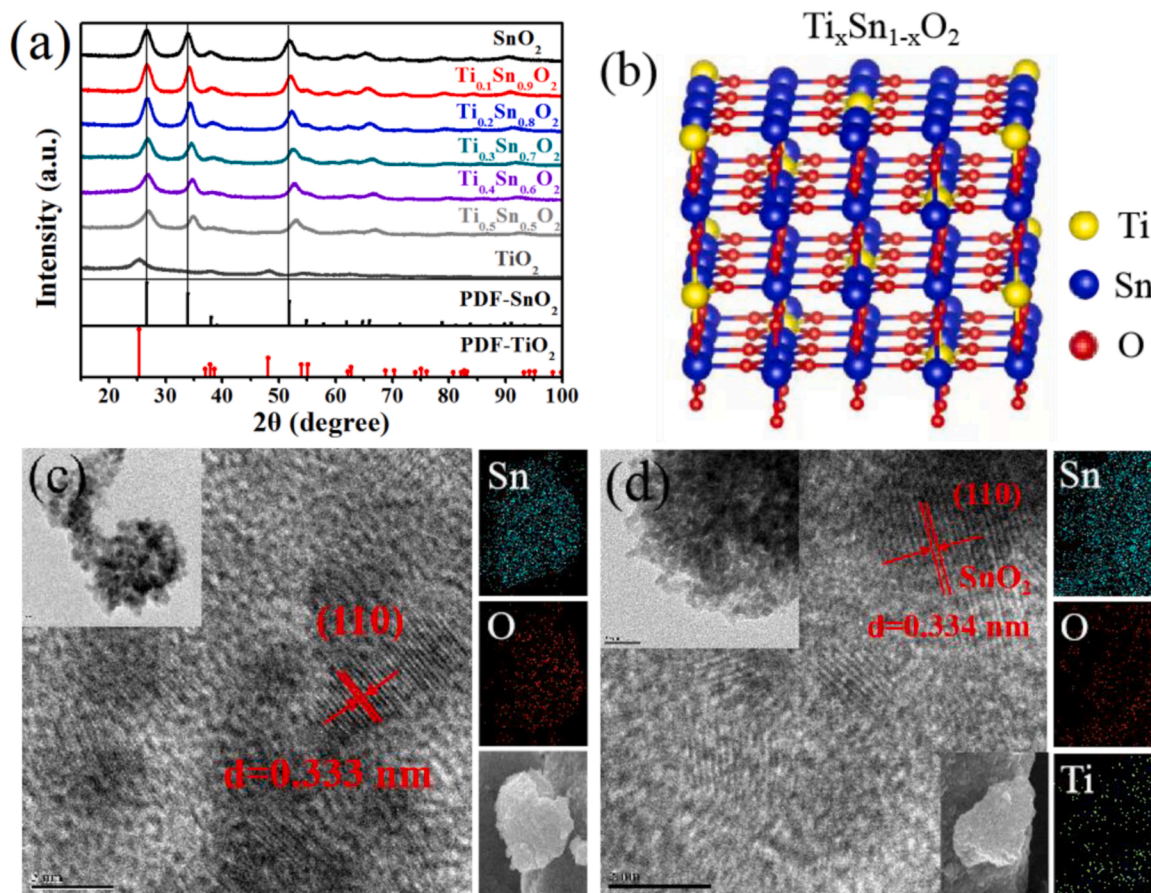


**Fig. 1.** (a) The XRD pattern of  $SnO_2$  and  $Ti_xSn_{1-x}O_2$ . (b) The crystal structure model of  $Ti_xSn_{1-x}O_2$ . The TEM, and SEM mapping images of (c)  $SnO_2$  and (d)  $Ti_{0.1}Sn_{0.9}O_2$ .



performed (Fig. S3). It can be clearly observed that the lattice parameter is significantly smaller, and the lattice spacing corresponding to  $\text{SnO}_2$  (110) facet is 0.302 nm, which further confirms that the introduction of Ti ions leads to smaller lattice parameters, consistent with XRD results. However, the lattice fringes of  $\text{TiO}_2$  could not be seen, indicating Ti ions form solid solutions with  $\text{SnO}_2$  rather than existing as separate  $\text{TiO}_2$  crystals. In addition, the elemental distribution shown in Fig. 1d also confirms that Ti is uniformly dispersed in  $\text{SnO}_2$ . In order to verify whether Ti ions are successfully introduced into the solid solution with high Ti concentration, TEM mapping and EDS analysis of  $\text{Ti}_{0.5}\text{Sn}_{0.5}\text{O}_2$  were carried out (Fig. S4). It can be seen that Ti is uniformly dispersed in  $\text{Ti}_{0.5}\text{Sn}_{0.5}\text{O}_2$ .

XPS spectra are used to analyze the surface composition and

chemical states of the prepared photocatalysts. It can be seen from Table S1 and Fig. S5 that there is no significant difference between the actual value and the theoretical value of Ti content in  $\text{Ti}_x\text{Sn}_{1-x}\text{O}_2$ , indicating the successful preparation of  $\text{Ti}_x\text{Sn}_{1-x}\text{O}_2$  solid solution. The XPS spectra of  $\text{SnO}_2$  and  $\text{Ti}_{0.1}\text{Sn}_{0.9}\text{O}_2$  are displayed in Fig. 2. Fig. 2a shows that  $\text{Ti}_{0.1}\text{Sn}_{0.9}\text{O}_2$  has obvious Ti 2p signal peak. It can be seen from Fig. 2b that there are two characteristic peaks at 495.3 and 486.8 eV, which are indexed as Sn 3d3/2 and Sn 3d5/2 of  $\text{SnO}_2$ , respectively [26]. In Sn 3d spectrum of  $\text{Ti}_{0.1}\text{Sn}_{0.9}\text{O}_2$  (Fig. 2c), the peaks at 487.3 eV and 495.7 eV correspond to  $\text{Sn}^{4+}$ , and the peaks at 486.7 eV and 495.2 eV correspond to  $\text{Sn}^{2+}$ . The existence of low valence state is attributed to the formation of oxygen vacancy caused by Ti ions introduction [27], which is consistent with the results of EPR test (Fig. S6). In

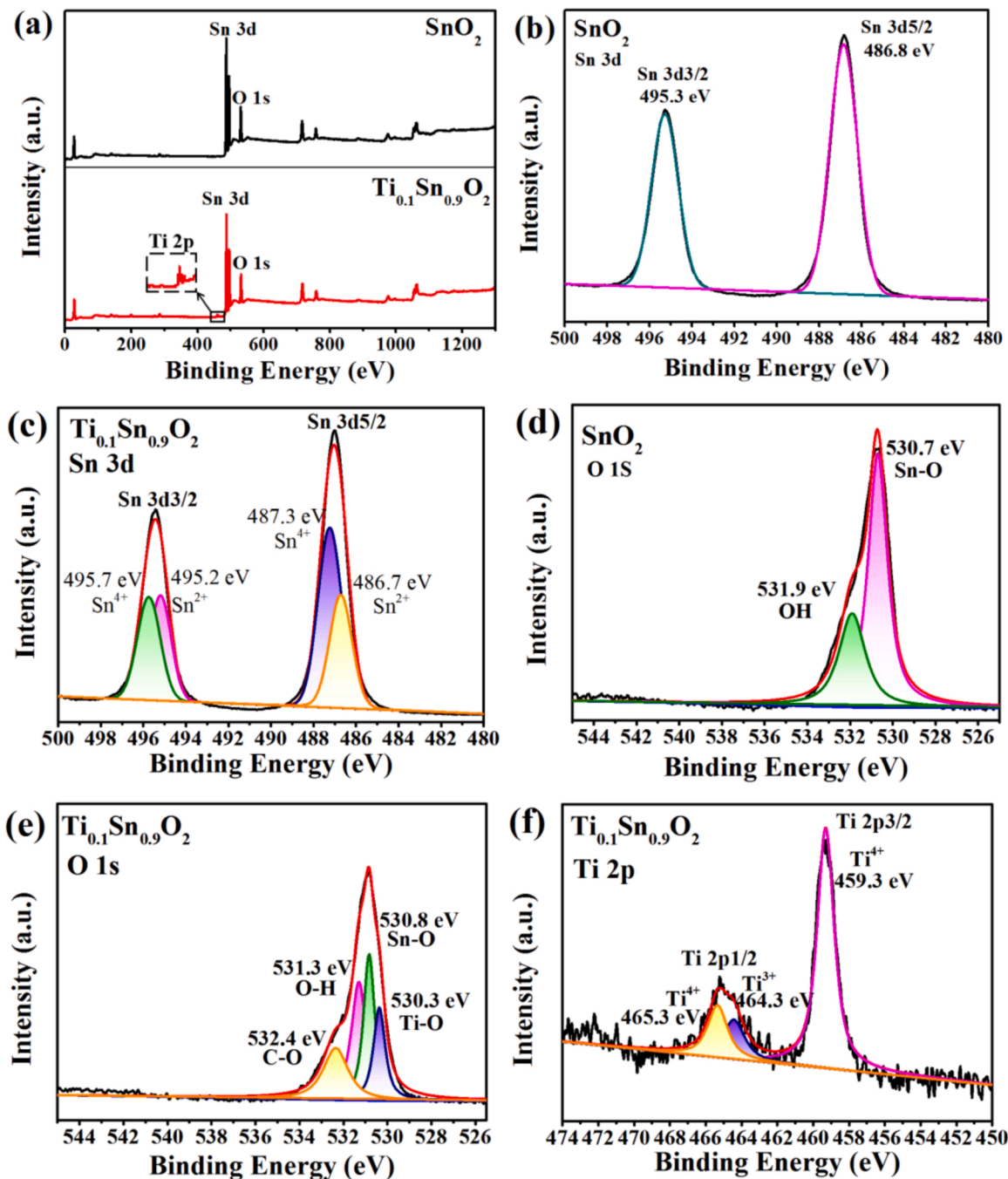


Fig. 2. (a) The XPS survey spectra of  $\text{SnO}_2$  and  $\text{Ti}_{0.1}\text{Sn}_{0.9}\text{O}_2$ . The Sn 3d spectrum of (b)  $\text{SnO}_2$  and (c)  $\text{Ti}_{0.1}\text{Sn}_{0.9}\text{O}_2$ . The O 1s spectrum of (d)  $\text{SnO}_2$  and (e)  $\text{Ti}_{0.1}\text{Sn}_{0.9}\text{O}_2$ . (f) The Ti 2p spectrum of  $\text{Ti}_{0.1}\text{Sn}_{0.9}\text{O}_2$ .



addition, the change of binding energy in Sn 3d spectra of SnO<sub>2</sub> and Ti<sub>0.1</sub>Sn<sub>0.9</sub>O<sub>2</sub> shows that the electronic properties of Sn sites are affected by Ti and O sites [28]. The O 1s energy spectrum of SnO<sub>2</sub> is shown in Fig. 2d, where the peaks at 531.9 eV and 530.7 eV match the O atoms in O-H and Sn-O bonds, respectively [20,29]. The O 1s energy spectrum of solid solution photocatalyst changed significantly. As shown in Fig. 2e, the signal peaks of Ti-O, Sn-O and H-O appear at 530.3 eV, 530.8 eV and 531.3 eV, respectively, and the C-O signal at 532.4 eV may be caused by the presence of oxygen vacancies [21,30]. In Ti 2p spectrum of Ti<sub>0.1</sub>Sn<sub>0.9</sub>O<sub>2</sub> (Fig. 2f), the peak at 459.3 eV corresponds to Ti 2p<sub>3/2</sub> of Ti<sup>4+</sup>, while the peaks at 464.3 eV and 465.3 eV correspond to Ti 2p<sub>1/2</sub> of Ti<sup>3+</sup> and Ti<sup>4+</sup>, respectively [31].

### 3.2. Photocatalytic toluene degradation performance

Under experimental conditions, the flow rate of synthetic air and N<sub>2</sub> are set to 95 mL/min and 9 mL/min, respectively. As shown in Fig. S1, the system humidity is maintained at approximately 50% by introducing one way synthetic air with 95 mL/min flow rate into deionized water. The toluene degradation performance of prepared SnO<sub>2</sub> and Ti<sub>x</sub>Sn<sub>1-x</sub>O<sub>2</sub> with different Sn/Ti ratios at 50% humidity are shown in Fig. S7. The introduction of Ti enhances the photocatalytic degradation ability of toluene and Ti<sub>0.1</sub>Sn<sub>0.9</sub>O<sub>2</sub> exhibits the highest degradation efficiency, which is also a high performance in current toluene degradation of flow system (Table S2). When Ti is introduced into SnO<sub>2</sub>, Ti-O-Sn active sites will be formed. In reaction process, the unique charge distribution around Ti-O-Sn active site can promote the activation of toluene. With the increase of Ti content, the Ti-O-Sn active site will be gradually covered by TiO<sub>2</sub>. When excessive Ti is added, the catalytic performance will gradually decline [32]. In addition, it can be clearly seen from

Fig. S7 and Fig. S8 that Ti<sub>0.1</sub>Sn<sub>0.9</sub>O<sub>2</sub> still maintains the best performance at 240 min. And with the increase of Ti content, the degradation efficiency first increased and then decreased. As for the increased degradation performance of Ti<sub>0.4</sub>Sn<sub>0.6</sub>O<sub>2</sub> and Ti<sub>0.5</sub>Sn<sub>0.5</sub>O<sub>2</sub>, it may be caused by surface defect sites, which is also confirmed by EPR test that Ti<sub>0.4</sub>Sn<sub>0.6</sub>O<sub>2</sub> and Ti<sub>0.5</sub>Sn<sub>0.5</sub>O<sub>2</sub> have large defect concentrations (Fig. S6). Moreover, the prepared Ti<sub>0.4</sub>Sn<sub>0.6</sub>O<sub>2</sub> and Ti<sub>0.5</sub>Sn<sub>0.5</sub>O<sub>2</sub> were treated in oxygen atmosphere at 150 °C for two hours to fill oxygen vacancy, and then the toluene degradation test was implemented. As shown in Fig. S9, the toluene degradation performance of Ti<sub>0.4</sub>Sn<sub>0.6</sub>O<sub>2</sub> and Ti<sub>0.5</sub>Sn<sub>0.5</sub>O<sub>2</sub> without vacancy is lower than that of original samples and also lower than Ti<sub>0.3</sub>Sn<sub>0.7</sub>O<sub>2</sub>, which proves the increased performance of Ti<sub>0.4</sub>Sn<sub>0.6</sub>O<sub>2</sub> and Ti<sub>0.5</sub>Sn<sub>0.5</sub>O<sub>2</sub> is caused by defects. The degradation difference between SnO<sub>2</sub> and Ti<sub>0.1</sub>Sn<sub>0.9</sub>O<sub>2</sub> is shown in Fig. 3a, which shows that the degradation efficiency of Ti<sub>0.1</sub>Sn<sub>0.9</sub>O<sub>2</sub> is 52% at 240 min, while that of SnO<sub>2</sub> is only 8%. Fig. 3b shows the mineralization ability of Ti<sub>0.1</sub>Sn<sub>0.9</sub>O<sub>2</sub> for toluene is also much higher than SnO<sub>2</sub> at 50% humidity. The mineralization yield of Ti<sub>0.1</sub>Sn<sub>0.9</sub>O<sub>2</sub> could reach 40% and 2.7 times that of SnO<sub>2</sub>, which can only reach about 15% after reaching stability. In addition, the toluene degradation test over P25 is implemented. It can be seen from Fig. S10 that there is a very serious inactivation phenomenon.

To investigate photocatalytic route, the effect of water vapor was studied. The humidity in the system is maintained at 0% while the initial concentration of toluene is kept unchanged for comparative test through isolating synthetic air from deionized water. As shown in Fig. 3c, the mineralization stability of Ti<sub>0.1</sub>Sn<sub>0.9</sub>O<sub>2</sub> decreases significantly when the humidity is 0%. Moreover, the mineralization yield of SnO<sub>2</sub> and Ti<sub>0.1</sub>Sn<sub>0.9</sub>O<sub>2</sub> are 10% and 20%, respectively. Compared with the presence of water vapor, the mineralization capacity of both SnO<sub>2</sub> and Ti<sub>0.1</sub>Sn<sub>0.9</sub>O<sub>2</sub> decreases while Ti<sub>0.1</sub>Sn<sub>0.9</sub>O<sub>2</sub> decreases more, which

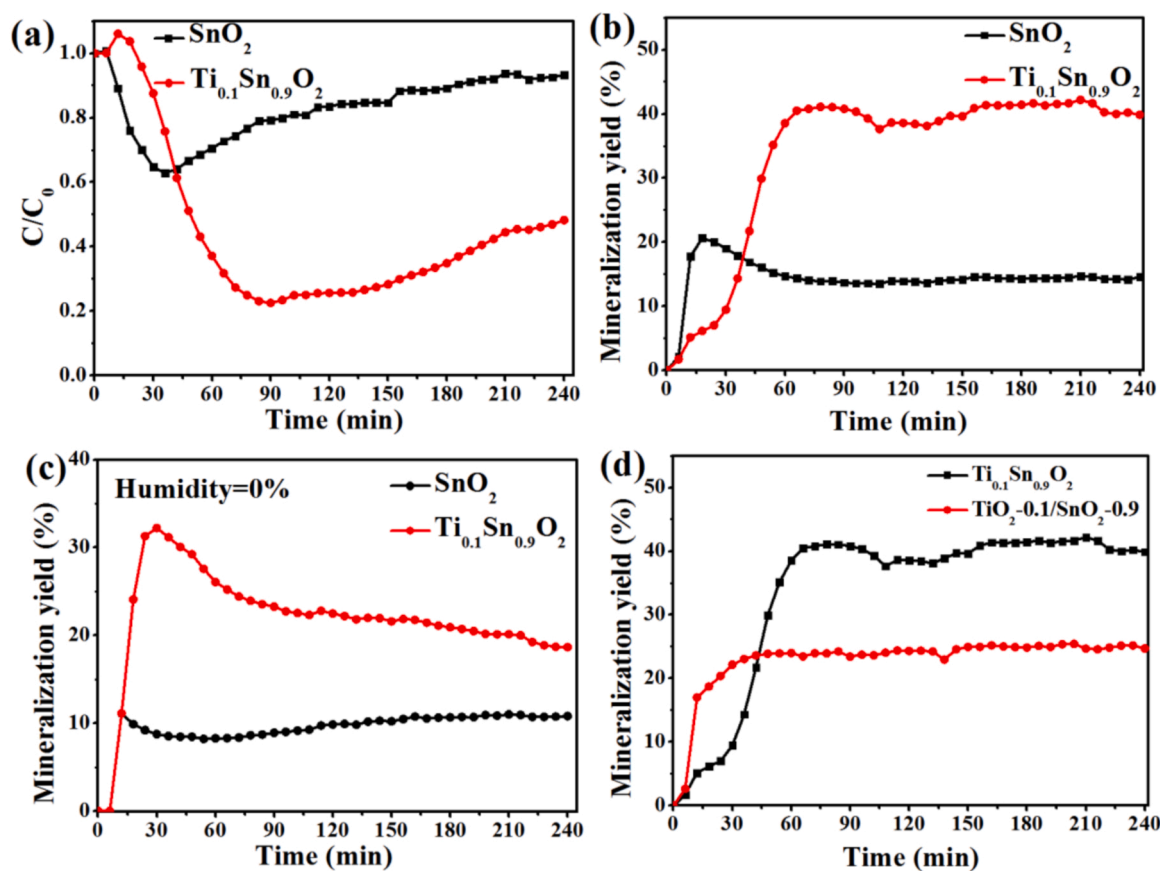


Fig. 3. (a) The curve of toluene concentration versus time in wet air; (b) The mineralization yield of toluene in wet air; (c) The mineralization yield of toluene in dry air under SnO<sub>2</sub> and Ti<sub>0.1</sub>Sn<sub>0.9</sub>O<sub>2</sub>. (d) The mineralization yield of toluene in wet air under Ti<sub>0.1</sub>Sn<sub>0.9</sub>O<sub>2</sub> and mechanically mixed SnO<sub>2</sub> and TiO<sub>2</sub>. All tests were carried out in flow reaction system at room temperature.

indicates that the presence of water vapor is conducive to the enhancement of toluene mineralization ability and  $\text{Ti}_{0.1}\text{Sn}_{0.9}\text{O}_2$  has stronger water molecular dependence. Importantly, the photocatalytic degradation ability of  $\text{Ti}_{0.1}\text{Sn}_{0.9}\text{O}_2$  for toluene is about twice that of mechanically mixed  $\text{SnO}_2$  and  $\text{TiO}_2$  in the same molar ratio (Fig. 3d), revealing the synergistic mechanism in the solid solution photocatalyst.

To investigate the reason of humidity-independence, contact angle was tested. The contact angle of  $\text{SnO}_2$  is  $22.1^\circ$ , higher than that of  $\text{Ti}_{0.1}\text{Sn}_{0.9}\text{O}_2$ , which is  $14.7^\circ$ , indicating that the surface of  $\text{Ti}_{0.1}\text{Sn}_{0.9}\text{O}_2$  has strong interaction with water molecules and that the introduction of Ti can enhance the water absorption of  $\text{SnO}_2$ . Therefore, the active sites on the surface of  $\text{Ti}_{0.1}\text{Sn}_{0.9}\text{O}_2$  will be more favorable to the dissociation of water molecules to produce more surface hydroxyl groups, which has a close positive correlation with photocatalytic activity. In order to further understand the mechanism of different materials on water molecules, the adsorption of water molecules on  $\text{SnO}_2$  and  $\text{Ti}_{0.1}\text{Sn}_{0.9}\text{O}_2$  is analyzed by theoretical simulation. As shown in Fig. 4, the adsorption energy of Sn ions away from Ti ions to water is  $-0.683$  eV, and that of Sn ions close to Ti ions is  $-0.802$  eV, showing the introduction of Ti ions enhances the adsorption of Sn ions to water, which is consistent with the experimental value. In addition, it can be seen from Fig. 4 and Fig. 9 that both Sn and Ti sites are more conducive to the adsorption of toluene than water molecules due to the more negative adsorption energy. Furthermore, the charge density difference ( $\Delta q$ ) of water molecules on Sn ions away from Ti and Sn ions close to Ti are  $-0.062$  e and  $-0.055$  e, respectively, revealing water molecules tend to give electrons [33] and Ti is more conducive to the adsorption of water molecules and Sn is more favorable to the activation of water molecules, which further indicates that there is a synergistic mechanism between Sn ions and Ti ions.

### 3.3. Generation of reactive oxygen species

$\text{O}_2$ -TPD test (Fig. 5) shows that there are two desorption peaks at about  $250^\circ\text{C}$  and  $450^\circ\text{C}$ . At lower desorption temperature, the adsorption capacity of oxygen increases first and then tends to be stable with the increase of Ti content, indicating the introduction of Ti can enhance the adsorption of oxygen in a certain range and also revealing that the adsorption of oxygen mainly occurs at the Ti site at lower reaction temperature. In addition, PL spectrum is used to analyze the carrier separation efficiency of  $\text{SnO}_2$  and solid solution photocatalysts [34]. It can be seen from Fig. 6 that the fluorescence peak intensity decreases significantly after the introduction of Ti ions, indicating solid solution photocatalysts have significantly enhanced carrier separation efficiency compared with pure  $\text{SnO}_2$ , which is beneficial to the

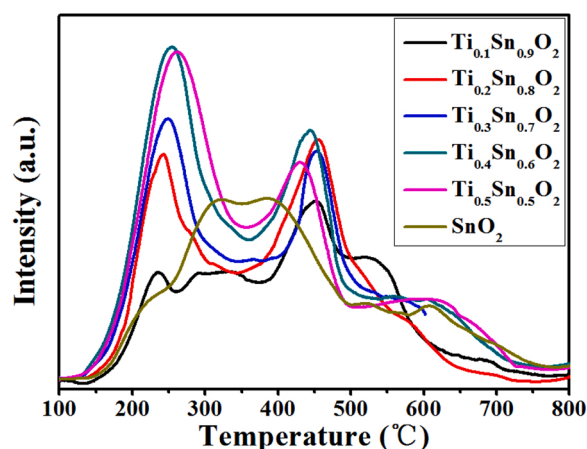


Fig. 5. The  $\text{O}_2$ -TPD test of  $\text{SnO}_2$  and  $\text{Ti}_x\text{Sn}_{1-x}\text{O}_2$ .

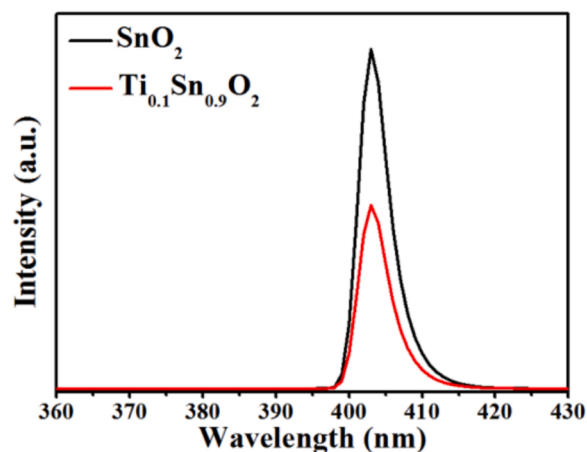


Fig. 6. The PL spectrum of  $\text{SnO}_2$  and  $\text{Ti}_{0.1}\text{Sn}_{0.9}\text{O}_2$ .

activation of molecular oxygen and the formation of reactive oxygen species. Photocurrent response (Fig. S11) and impedance spectra (Fig. S12) also confirmed that the introduction of Ti enhanced spatial charge separation.

The difference of reactive oxygen species produced by different

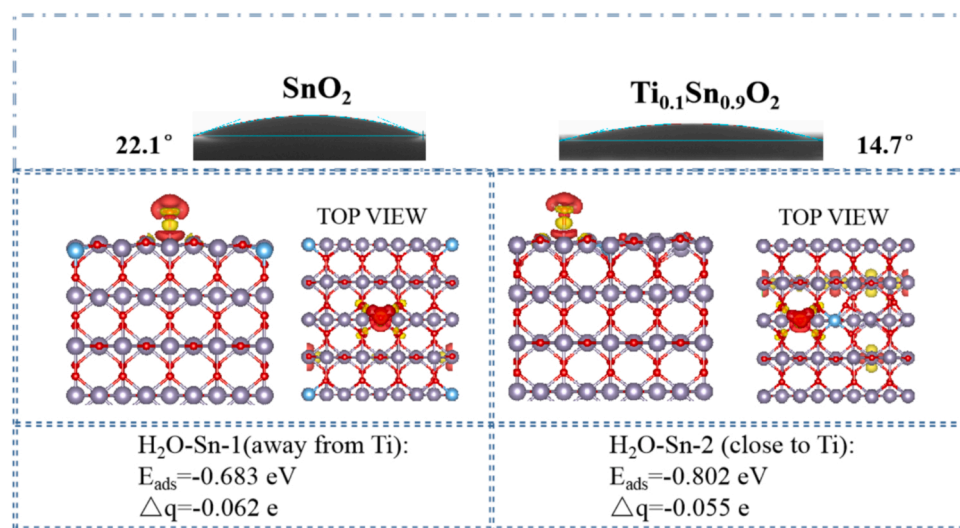


Fig. 4. The contact angle of water on  $\text{SnO}_2$  and  $\text{Ti}_{0.1}\text{Sn}_{0.9}\text{O}_2$  surface, and the adsorption model of water molecules.

photocatalysts is confirmed by EPR spin capture experiment (Fig. 7). The 5, 5-dimethyl-1-pyrroline-n-oxide (DMPO) trapping agent could react with superoxide radicals ( $\bullet\text{O}_2^-$ ) to produce the specific characteristic peak of 1:1:1:1, while reacts with hydroxyl radicals ( $\bullet\text{OH}$ ) to produce 1:2:2:1 characteristic peak [35]. As shown in Fig. 7a,  $\text{SnO}_2$  and  $\text{Ti}_{0.1}\text{Sn}_{0.9}\text{O}_2$  have no signal peaks under dark condition.  $\text{Ti}_{0.1}\text{Sn}_{0.9}\text{O}_2$  has an obvious four line characteristic peak with a ratio of 1:1:1:1 under illumination condition, which corresponds to the characteristic signal of  $\bullet\text{O}_2^-$ . However, no  $\bullet\text{O}_2^-$  signal is detected in  $\text{SnO}_2$  under illumination condition. These results reveal that  $\text{Ti}_{0.1}\text{Sn}_{0.9}\text{O}_2$  solid solution can lead to the production of  $\bullet\text{O}_2^-$ , while  $\text{SnO}_2$  cannot. It can be seen from Fig. 7b that both  $\text{SnO}_2$  and  $\text{Ti}_{0.1}\text{Sn}_{0.9}\text{O}_2$  produce characteristic signals with a ratio of 1:2:2:1 under illumination condition, indicating that both  $\text{SnO}_2$  and  $\text{Ti}_{0.1}\text{Sn}_{0.9}\text{O}_2$  can produce  $\bullet\text{OH}$ . Moreover, the signal peak intensity generated by  $\text{Ti}_{0.1}\text{Sn}_{0.9}\text{O}_2$  is significantly higher than that of  $\text{SnO}_2$ , revealing that  $\text{Ti}_{0.1}\text{Sn}_{0.9}\text{O}_2$  could produce more  $\bullet\text{OH}$  and solid solution photocatalyst is more conducive to the activation of molecular oxygen.

### 3.4. Determination of energy bands positions

The light absorption and band gap are measured by DRS test. It can be seen from Fig. 8a that the light absorption range redshifts after the introduction of Ti ions and  $\text{Ti}_{0.1}\text{Sn}_{0.9}\text{O}_2$  has the most excellent visible light absorption. Since  $\text{SnO}_2$  is a direct semiconductor [36], according to the formula  $\alpha(h\nu) = N(h\nu - E_g)^{n/2}$  ( $\alpha$ ,  $N$ ,  $\nu$ ,  $h$ , and  $E_g$  represent the absorbance, constant, optical frequency, planck constant, and band gap energy, respectively. When catalyst is a direct semiconductor,  $n = 1$ ; when catalyst is an indirect semiconductor,  $n = 4$ ) [37], the intersection of X axis and tangent of curve in the diagram of  $(\alpha h\nu)^2$  relative to  $h\nu$  (Fig. 8b) is  $E_g$ . As can be seen from Fig. 8b, the  $E_g$  of  $\text{SnO}_2$  and  $\text{Ti}_{0.1}\text{Sn}_{0.9}\text{O}_2$  are 3.50 eV and 3.24 eV, respectively. Furthermore, Mott-Schottky test is used to determine the flat band potential of photocatalyst [38]. It can be seen from Fig. 8c that the flat band potential of  $\text{SnO}_2$  and  $\text{Ti}_{0.1}\text{Sn}_{0.9}\text{O}_2$  relative to Ag/AgCl electrode are  $-0.62$  V and  $-0.87$  V, respectively. Since the flat band potential relative to standard hydrogen electrode could be obtained according to the formula  $E_{\text{RHE}} = E^\circ_{\text{Ag/AgCl}} + E_{\text{Ag/AgCl}} + 0.059 \text{ pH}$  ( $\text{pH} = 6.8$ ,  $E^\circ_{\text{Ag/AgCl}} = 0.199$  V) [39], the flat band potential of  $\text{SnO}_2$  and  $\text{Ti}_{0.1}\text{Sn}_{0.9}\text{O}_2$  relative to the standard hydrogen electrode are  $-0.02$  V and  $-0.27$  V, respectively. Since the conduction band potential ( $E_{\text{CB}}$ ) of n-type semiconductor is close to the flat band potential relative to standard hydrogen electrode [40], the  $E_{\text{CB}}$  of  $\text{SnO}_2$  and  $\text{Ti}_{0.1}\text{Sn}_{0.9}\text{O}_2$  can be approximately represented by the flat band potential, which are  $-0.02$  V and  $-0.27$  V, respectively. The valence band potential ( $E_{\text{VB}}$ ) of photocatalyst can be obtained according to the formula  $E_{\text{VB}} = E_{\text{CB}} + E_g$  [41]. Therefore, the  $E_{\text{VB}}$  of  $\text{SnO}_2$  and  $\text{Ti}_{0.1}\text{Sn}_{0.9}\text{O}_2$  are 3.48 V and 2.97 V, respectively. The obtained energy band structure is shown in Fig. 8d. The introduction of Ti ions reduces

the band gap of  $\text{SnO}_2$ , and the band gap of  $\text{Ti}_{0.1}\text{Sn}_{0.9}\text{O}_2$  is 0.26 eV lower than that of pure  $\text{SnO}_2$ . Moreover, the conduction band position of solid solution photocatalyst is significantly improved. As the electrode potential of  $\text{O}_2/\bullet\text{O}_2^-$  relative to standard hydrogen electrode is  $-0.046$  V [42],  $\text{SnO}_2$  cannot activate molecular oxygen to generate  $\bullet\text{O}_2^-$  due to lower conduction band position, while  $\text{Ti}_{0.1}\text{Sn}_{0.9}\text{O}_2$  can generate  $\bullet\text{O}_2^-$ , which is consistent with the detection results of DMPO- $\bullet\text{O}_2^-$  in Fig. 7a. Since the electrode potentials of  $\text{H}_2\text{O}/\bullet\text{OH}$  and  $\text{OH}^-/\bullet\text{OH}$  relative to standard hydrogen electrode are 2.34 V and 2.38 V, respectively [43, 44], both  $\text{SnO}_2$  and  $\text{Ti}_{0.1}\text{Sn}_{0.9}\text{O}_2$  can oxidize  $\text{H}_2\text{O}$  or  $\text{OH}^-$  to generate  $\bullet\text{OH}$  due to their low valence band positions, which is also consistent with the result of EPR spin capture experiment in Fig. 7b.

The adsorption of toluene molecules on the Sn and Ti sites in solid solution photocatalyst is analyzed by DFT calculations. As shown in Fig. 9, the adsorption energy of toluene molecules on Sn and Ti sites in  $\text{Ti}_{0.1}\text{Sn}_{0.9}\text{O}_2$  are  $-0.922$  eV and  $-0.936$  eV, respectively, indicating toluene molecules can be spontaneously adsorbed on Sn and Ti sites, and the Ti sites are more favorable for toluene adsorption. In addition, the charge density difference ( $\Delta q$ ) of toluene molecules on Sn and Ti sites are  $-0.03\text{e}$  and  $-0.01\text{e}$ , respectively, where negative values imply that toluene molecules tend to transfer electrons to the surface of catalyst. The more negative charge density difference and stronger electron cloud density near Sn sites indicate that Sn sites are more conducive to the activation of toluene molecule. The above theoretical analysis confirms the synergistic mechanism of Sn and Ti sites on toluene mineralization reaction.

### 3.5. Photocatalytic toluene mineralization routes

In situ DRIFT spectroscopy is used to monitor the intermediate products of toluene mineralization reaction. Figs. 10a and 10b are vibrational absorption spectra of intermediate products on  $\text{SnO}_2$  surface under dark and illumination conditions, respectively. It can be seen from Fig. 10a that the absorption vibration peaks appear at  $3606 \text{ cm}^{-1}$  and  $3459 \text{ cm}^{-1}$  under dark condition, which correspond to the absorption vibration of benzyl alcohol [45], and a small amount of absorption vibration of benzoic acid ( $1541 \text{ cm}^{-1}$ ) is also detected [46], implying that the spontaneous exothermic process of toluene on the surface of  $\text{SnO}_2$  under dark condition. However, this conversion process is less, especially the conversion of benzoic acid, which can be basically ignored. Under illumination condition (Fig. 10b), the signal peak of benzyl alcohol ( $3566 \text{ cm}^{-1}$ ) is detected in the first few minutes [47]. The slight difference in the absorption vibration peaks of benzyl alcohol under illumination and dark conditions may be attributed to the chemical bonds activation of benzyl alcohol caused by light, resulting in the elongation or rotation of chemical bonds. With the extension of illumination time, the vibration signal of benzyl alcohol decreased gradually,

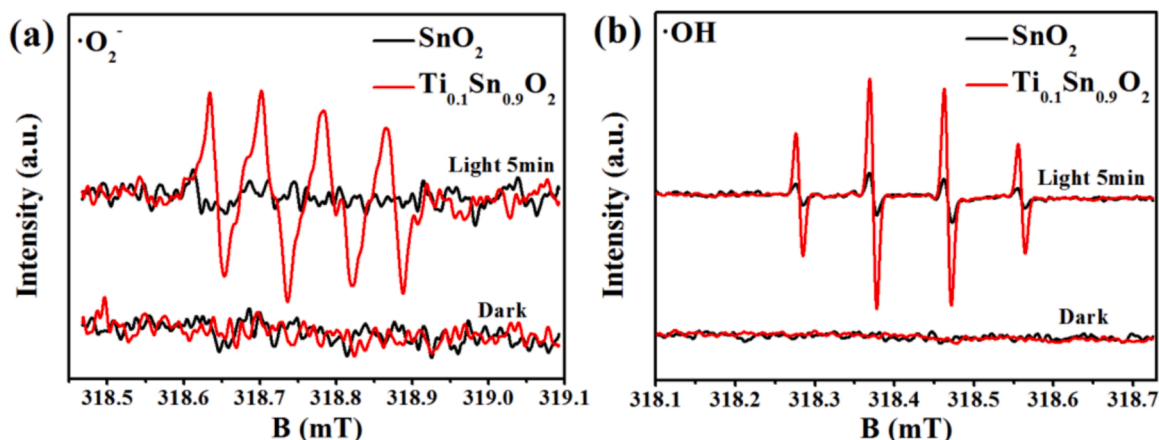


Fig. 7. The (a) DMPO- $\bullet\text{O}_2^-$  and (b) DMPO- $\bullet\text{OH}$  EPR spin capture spectra of  $\text{SnO}_2$  and  $\text{Ti}_{0.1}\text{Sn}_{0.9}\text{O}_2$ .



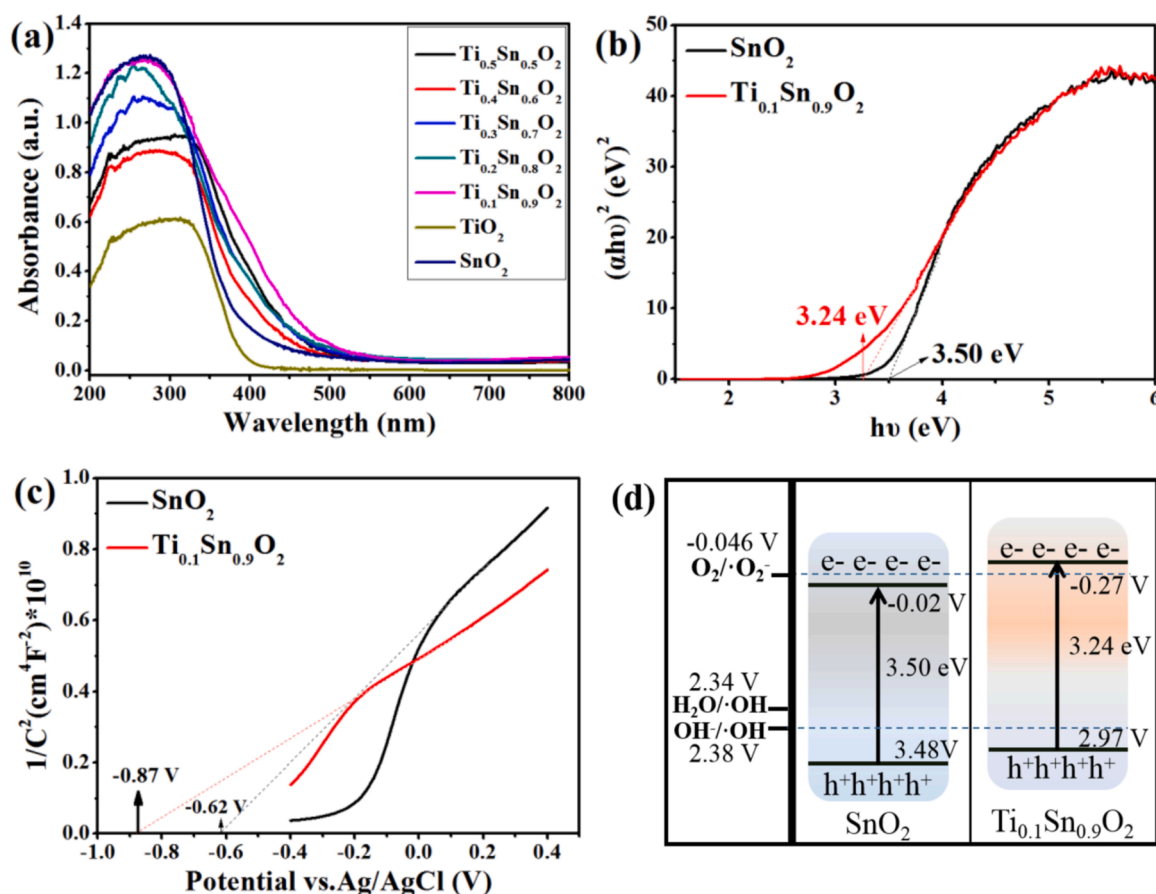


Fig. 8. (a) The DRS spectrum of  $\text{SnO}_2$  and  $\text{Ti}_x\text{Sn}_{1-x}\text{O}_2$ . The (b) Eg; (c) Mott-Schottky test; and (d) Energy band structure of  $\text{SnO}_2$  and  $\text{Ti}_{0.1}\text{Sn}_{0.9}\text{O}_2$ .

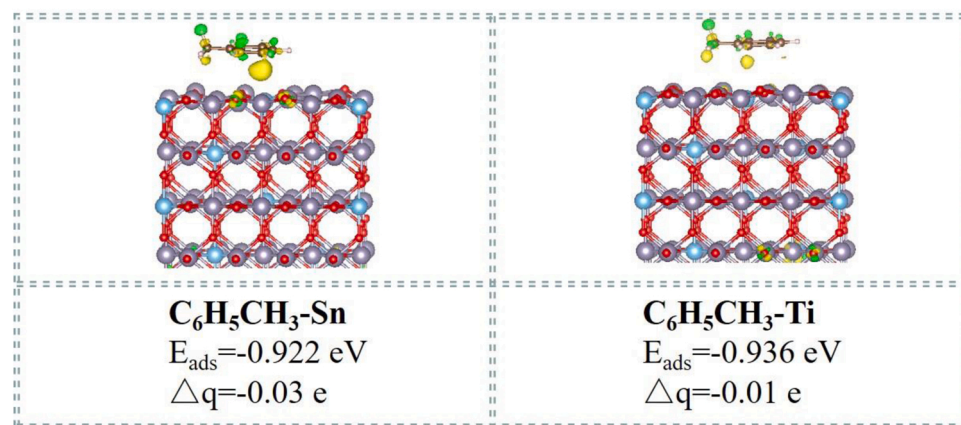


Fig. 9. The adsorption model of toluene on Sn and Ti sites in solid solution photocatalyst.

indicating the diminish of benzyl alcohol. Moreover, no vibration absorption signal of other intermediates is detected such as benzaldehyde and benzoic acid, which may be attributed to the lack of superoxide radicals, implying benzyl alcohol will not be further converted, but will be directly ring-opened on the surface of  $\text{SnO}_2$  under illumination. The truncated part of the 3250–1750  $\text{cm}^{-1}$  range is a strong  $\text{CO}_2$  signal peak. The relatively low adsorption intensity of benzyl alcohol under illumination condition may be attributed to the high  $\text{CO}_2$  peak intensity. Fig. 10c shows the vibrational absorption spectra of intermediates products on  $\text{Ti}_{0.1}\text{Sn}_{0.9}\text{O}_2$  surface under dark condition. Benzyl alcohol (3605  $\text{cm}^{-1}$ ) [48], benzaldehyde (1630  $\text{cm}^{-1}$ ) [49] and few benzoic acid (1496  $\text{cm}^{-1}$ ) [45] are detected, and the amount of these

intermediates gradually increased with the increase of adsorption time, indicating that toluene is mainly converted to benzyl alcohol and benzaldehyde due to spontaneous exothermic process on the surface of  $\text{Ti}_{0.1}\text{Sn}_{0.9}\text{O}_2$  under dark condition. Moreover, Sn-O-Ti active site in  $\text{Ti}_{0.1}\text{Sn}_{0.9}\text{O}_2$  is more favorable to convert toluene to benzaldehyde than  $\text{SnO}_2$ . Fig. 10d shows the vibrational absorption spectra on the surface of  $\text{Ti}_{0.1}\text{Sn}_{0.9}\text{O}_2$  under illumination. The vibrational absorption peaks of benzoic acid and a small amount of benzyl alcohol appear at 1542  $\text{cm}^{-1}$  and 1362  $\text{cm}^{-1}$ , respectively [46,50], indicating benzoic acid is the main intermediate product on  $\text{Ti}_{0.1}\text{Sn}_{0.9}\text{O}_2$  under illumination, which then undergoes ring-opening reaction. The signal at  $\sim 3500$   $\text{cm}^{-1}$  can hardly be detected over  $\text{Ti}_{0.1}\text{Sn}_{0.9}\text{O}_2$  may be attributed to the rapid

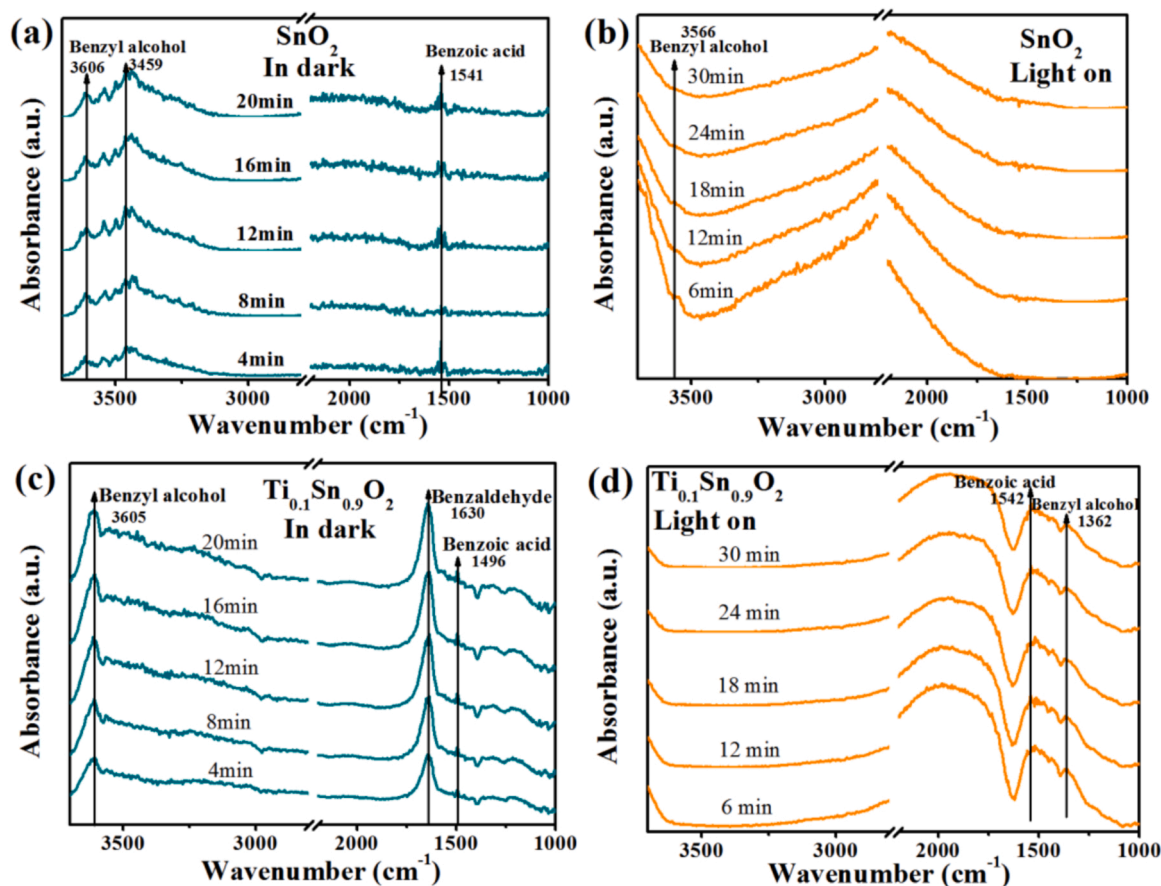


Fig. 10. The in situ DRIFT spectroscopy of SnO<sub>2</sub> and Ti<sub>0.1</sub>Sn<sub>0.9</sub>O<sub>2</sub> under (a) and (c) dark condition; and under (b) and (d) illumination condition.

conversion of -OH [47]. Notely, under illumination condition, a large amount of benzoic acid is detected in Ti<sub>0.1</sub>Sn<sub>0.9</sub>O<sub>2</sub>, which is not detected in SnO<sub>2</sub>, indicating superoxide radicals play an important role in the generation of benzoic acid. As for benzaldehyde can hardly be detected on Ti<sub>0.1</sub>Sn<sub>0.9</sub>O<sub>2</sub> under illumination condition, suggesting it is rapidly oxidized to benzoic acid with the participation of superoxide radicals.

The photocatalytic toluene conversion mechanism on different photocatalysts under illumination are shown in Fig. 11a. In SnO<sub>2</sub>, •OH plays a decisive role in the reaction mechanism, which will attack the methyl group on toluene to produce benzyl alcohol, and the absence of phenolic intermediates may be attributed to the fact that holes are hardly involved in the reaction due to the high thermodynamic energy is mainly used for water oxidation reaction to generate •OH [51]. Subsequently, benzyl alcohol undergoes ring-opening reaction and eventually decomposes into carbon dioxide and water. In solid solution photocatalyst, •OH and •O<sub>2</sub> play an important role in reaction process because both hydroxyl radical and superoxide radical could be generated. Firstly, hydroxyl radical attacks methyl group to realize the conversion from toluene to benzyl alcohol, and then it is oxidized to benzoic acid under the action of superoxide radical. In SnO<sub>2</sub> and solid solution catalysts, hydroxyl radicals are used for the conversion of toluene to benzyl alcohol on the one hand, and for the ring opening reaction on the other hand. However, toluene can only be converted to and benzoic acid with the participation of superoxide radicals, which can be realized in solid solution catalysts. Therefore, the ring-opening reaction of benzyl alcohol occurs in SnO<sub>2</sub>, while the ring-opening reaction of benzoic acid takes place in solid solution photocatalyst. After ring opening, the carbon-carbon bond is broken to generate formate and acetone, etc., and finally generates CO<sub>2</sub> and water [52]. In addition, the reaction path of toluene on Ti<sub>0.1</sub>Sn<sub>0.9</sub>O<sub>2</sub> is more promising according to Fig. S13. As shown in Fig. 11b, theoretical analysis confirms that the activation

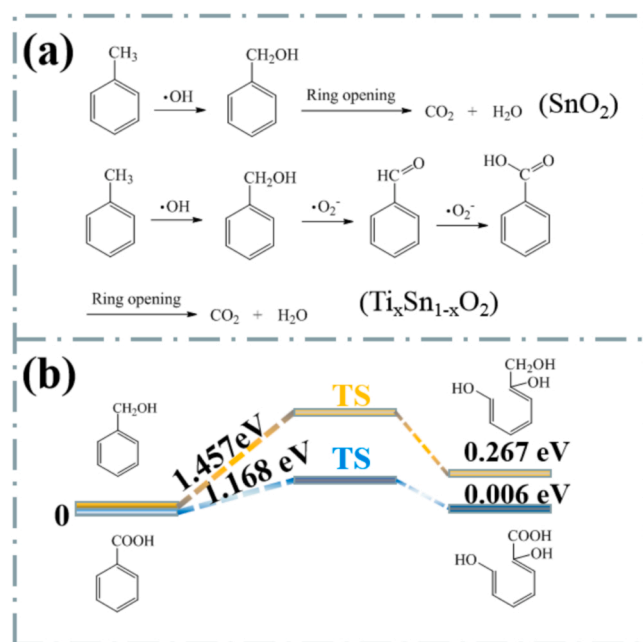


Fig. 11. The reaction and ring opening pathways.

energy and reaction energy of the ring-opening reaction of benzyl alcohol are 1.457 eV and 0.267 eV, while the activation energy and reaction energy of benzoic acid ring-opening are 1.168 eV and 0.006 eV, respectively. The activation energy of benzoic acid is 0.289 eV lower

than that of benzyl alcohol, indicating that benzoic acid has lower ring-opening barrier and is more prone to ring opening reaction. Therefore, the higher degradation and mineralization yield of toluene in  $\text{Ti}_x\text{Sn}_{1-x}\text{O}_2$  solid solution photocatalyst are attributed to the fact that the intermediate product is mainly benzoic acid, which has low ring-opening energy barrier. And the poor toluene mineralization yield of  $\text{SnO}_2$  is mainly due to the presence of benzyl alcohol with high ring-opening energy barrier.

#### 4. Conclusions

In summary,  $\text{SnO}_2$  and  $\text{Ti}_x\text{Sn}_{1-x}\text{O}_2$  solid solution photocatalyst are prepared for the study of photocatalytic degradation mechanism of toluene. After Ti ions is introduced, the synergistic effect of Sn and Ti sites enhances the activation of water and toluene molecules, which significantly improves the mineralization performance of toluene. Moreover, the removal performance of toluene has been greatly improved in wet environment. The introduction of Ti ions shifts the conduction band position upward, resulting in the generation of superoxide radicals in the solid solution photocatalyst, followed by selective formation of benzyl alcohol and benzoic acid from toluene on the surface of  $\text{SnO}_2$  and  $\text{Ti}_x\text{Sn}_{1-x}\text{O}_2$ , respectively. Benzoic acid has lower ring opening barrier, which makes the solid solution photocatalyst more conducive to the mineralization of toluene. This work provides a way to regulate the ability of photocatalysts through reactive oxygen radical, reveals the reactive oxygen species-dependent toluene mineralization reaction mechanism, and offers reference for photocatalyst design from the viewpoint of radicals, instead of traditional photo-absorption and separation efficiency.

#### CRediT authorship contribution statement

**Qi Li:** Investigation, Methodology, Data curation, Writing – original draft. **Zi-han Yue:** Investigation, Data curation. **Mi-sha Shan:** Investigation, Data curation, Validation. **Yi-lei Li:** Theoretical calculation, Formal analysis. **Ying-juan Hao:** Formal analysis, Validation. **Ying Liu:** Investigation, Formal analysis. **Fa-tang Li:** Conceptualization, Methodology, Writing – review & editing, Supervision, Project administration, Funding acquisition.

#### Declaration of Competing Interest

The authors declare that they have no known competing financial interests or personal relationships that could have appeared to influence the work reported in this paper.

#### Data availability

Data will be made available on request.

#### Acknowledgements

This work was financially supported by National Natural Science Foundation of China (21776059, 22178084, 51802076), and the Foundation for Innovative Research Groups of the Natural Science Foundation of Hebei Province (No. B2021208005).

#### Appendix A. Supporting information

Supplementary data associated with this article can be found in the online version at [doi:10.1016/j.apcatb.2023.122628](https://doi.org/10.1016/j.apcatb.2023.122628).

#### References

- [1] J. Jin, P. Li, D.H. Chun, B. Jin, K. Zhang, J.H. Park, Defect dominated hierarchical Ti-metal-organic frameworks via a linker competitive coordination strategy for

- toluene removal, *Adv. Funct. Mater.* 31 (2021) 2102511, <https://doi.org/10.1002/adfm.202102511>.
- [2] K. Su, H. Liu, B. Zeng, Z. Zhang, N. Luo, Z. Huang, Z. Gao, F. Wang, Visible-light-driven selective oxidation of toluene into benzaldehyde over nitrogen-modified  $\text{Nb}_2\text{O}_5$  nanomeses, *ACS Catal.* 10 (2020) 1324–1333, <https://doi.org/10.1021/acscatal.9b04215>.
- [3] J. Li, X. Dong, G. Zhang, W. Cui, W. Cen, Z. Wu, S. Lee, F. Dong, Probing ring-opening pathways for efficient photocatalytic toluene decomposition, *J. Mater. Chem. A* 7 (2019) 3366–3374, <https://doi.org/10.1039/c8ta11627j>.
- [4] X. Wang, Y. Zhang, C. Zhou, D. Huo, R. Zhang, L. Wang, Hydroxyl-regulated BiOI nanosheets with a highly positive valence band maximum for improved visible-light photocatalytic performance, *Appl. Catal. B Environ.* 268 (2020), 118390, <https://doi.org/10.1016/j.apcatb.2019.118390>.
- [5] F. Ghanbari, M. Eskandari, P. Nazari, S. Gharibzadeh, S. Kohnepoushi, B. A. Nejand, Potential continuous removal of toluene by ZnO nanorods grown on permeable alumina tube filters, *RSC Adv.* 6 (2016) 52360–52371, <https://doi.org/10.1039/c6ra07801j>.
- [6] R. Xie, D. Lei, Y. Zhan, B. Liu, C.H.A. Tsang, Y. Zeng, K. Li, D.Y.C. Leung, H. Huang, Efficient photocatalytic oxidation of gaseous toluene over F-doped  $\text{TiO}_2$  in a wet scrubbing process, *Chem. Eng. J.* 386 (2020), 121025, <https://doi.org/10.1016/j.cej.2019.02.112>.
- [7] D. Tsukamoto, Y. Shiraishi, T. Hirai, Selective side-chain oxidation of alkyl-substituted aromatics on  $\text{TiO}_2$  partially coated with  $\text{WO}_3$  as a photocatalyst, *Catal. Sci. Technol.* 3 (2013) 2270–2277, <https://doi.org/10.1039/c3cy00219e>.
- [8] W. Wu, Y. Song, L. Bai, Z. Chen, H. Sun, G. Zhen, R. Zhan, Y. Shen, J. Qian, Q. Yuan, Z. Sun, Graphene oxide-BiOCl nanoparticle composites as catalysts for oxidation of volatile organic compounds in nonthermal plasmas, *ACS Appl. Nano Mater.* 3 (2020) 9363–9374, <https://doi.org/10.1021/acsnm.0c01994>.
- [9] X. Li, T. Wang, X. Tao, G. Qiu, C. Li, B. Li, Interfacial synergy of Pd sites and defective BiOBr for promoting the solar-driven selective oxidation of toluene, *J. Mater. Chem. A* 8 (2020) 17657–17669, <https://doi.org/10.1039/d0ta05733a>.
- [10] R. Sun, Q. Shi, M. Zhang, L. Xie, J. Chen, X. Yang, M. Chen, W. Zhao, Enhanced photocatalytic oxidation of toluene with a coral-like direct Z-scheme  $\text{BiVO}_4/\text{g-C}_3\text{N}_4$  photocatalyst, *J. Alloy. Compd.* 714 (2017) 619–626, <https://doi.org/10.1016/j.jallcom.2017.04.108>.
- [11] H. Li, F. Jiang, S. Drdova, H. Shang, L. Zhang, J. Wang, Dual-function surface hydrogen bonds enable robust  $\text{O}_2$  activation for deep photocatalytic toluene oxidation, *Catal. Sci. Technol.* 11 (2021) 319–331, <https://doi.org/10.1039/d0cy01907k>.
- [12] Q. Zhang, F. Li, X. Chang, D. He, Comparison of nickel foam/Ag-supported ZnO,  $\text{TiO}_2$ , and  $\text{WO}_3$  for toluene photodegradation, *Mater. Manuf. Process.* 29 (2014) 789–794, <https://doi.org/10.1080/10426914.2014.892616>.
- [13] L. Chen, W. Cui, J. Li, H. Wang, X. Dong, P. Chen, Y. Zhou, F. Dong, The high selectivity for benzoic acid formation on  $\text{Ca}_2\text{Sb}_2\text{O}_7$  enables efficient and stable toluene mineralization, *Appl. Catal. B Environ.* 271 (2020), 118948, <https://doi.org/10.1016/j.apcatb.2020.118948>.
- [14] S. Anuchai, S. Phanichphant, D. Tantraviwat, P. Pluegphon, T. Bovornratanarak, B. Inceesungvorn, Low temperature preparation of oxygen-deficient tin dioxide nanocrystals and a role of oxygen vacancy in photocatalytic activity improvement, *J. Colloid Interface Sci.* 512 (2018) 105–114, <https://doi.org/10.1016/j.jcis.2017.10.047>.
- [15] L. Li, G. Liu, S. Qi, X. Liu, L. Gu, Y. Lou, J. Chen, Y. Zhao, Highly efficient colloidal  $\text{Mn}_2\text{Cd}_{1-x}\text{S}$  nanorod solid solution for photocatalytic hydrogen generation, *J. Mater. Chem. A* 6 (2018) 23683, <https://doi.org/10.1039/c8ta08458k>.
- [16] L. Ye, C. Han, Z. Ma, Y. Leng, J. Li, X. Ji, D. Bi, H. Xie, Z. Huang, Ni<sub>2</sub>P loading on  $\text{Cd}_0.5\text{Zn}_{0.5}\text{S}$  solid solution for exceptional photocatalytic nitrogen fixation under visible light, *Chem. Eng. J.* 307 (2017) 311–318, <https://doi.org/10.1016/j.cej.2016.08.102>.
- [17] J. Huang, D. Li, R. Li, P. Chen, Q. Zhang, H. Liu, W. Lv, G. Liu, Y. Feng, One-step synthesis of phosphorus/oxygen co-doped  $\text{g-C}_3\text{N}_4/\text{anatase TiO}_2$  Z-scheme photocatalyst for significantly enhanced visible-light photocatalysis degradation of enrofloxacin, *J. Hazard. Mater.* 386 (2020), 121634, <https://doi.org/10.1016/j.jhazmat.2019.121634>.
- [18] L.Q. Wei, B.H. Ye, Cyclometalated Ir-Zr Metal-organic frameworks as recyclable visible-light photocatalysts for sulfide oxidation into sulfoxide in water, *ACS Appl. Mater. Interfaces* 11 (2019) 41448–41457, <https://doi.org/10.1021/acsaami.9b15646>.
- [19] Q. Li, J. Ren, Y. Hao, Y. Li, X. Wang, Y. Liu, R. Su, F. Li, Insight into reactive species-dependent photocatalytic toluene mineralization and deactivation pathways via modifying hydroxyl groups and oxygen vacancies on BiOCl, *Appl. Catal. B Environ.* 317 (2022), 121761, <https://doi.org/10.1016/j.apcatb.2022.121761>.
- [20] R. Chen, J. Li, J. Sheng, W. Cui, X. Dong, P. Chen, H. Wang, Y. Sun, F. Dong, Unveiling the unconventional roles of methyl number on the ring-opening barrier in photocatalytic decomposition of benzene, toluene and o-xylene, *Appl. Catal. B Environ.* 278 (2020), 119318, <https://doi.org/10.1016/j.apcatb.2020.119318>.
- [21] Q. Tian, W. Wei, J. Dai, Q. Sun, J. Zhuang, Y. Zheng, P. Liu, M. Fan, L. Chen, Porous Core-shell  $\text{Ti}_x\text{Sn}_{1-x}\text{O}_2$  solid solutions with broad-light response: one-pot synthesis and ultrahigh photooxidation performance, *Appl. Catal. B Environ.* 244 (2019) 45–55, <https://doi.org/10.1016/j.apcatb.2018.11.045>.
- [22] G. Kresse, J. Furthmüller, Efficient iterative schemes for ab initio total-energy calculations using a plane-wave basis set, *Phys. Rev. B* 54 (1996) 11169–11186, <https://doi.org/10.1103/PhysRevB.54.11169>.
- [23] J.P. Perdew, K. Burke, M. Ernzerhof, Generalized gradient approximation made simple, *Phys. Rev. Lett.* 77 (1996) 3865–3868, <https://doi.org/10.1103/PhysRevLett.77.3865>.



- [24] S. Grimme, J. Antony, S. Ehrlich, H. Krieg, A consistent and accurate ab initio parametrization of density functional dispersion correction (DFT-D) for the 94 elements H-Pu, *J. Chem. Phys.* 132 (2010), 154104, <https://doi.org/10.1063/1.3382344>.
- [25] R. Shi, H. Ye, F. Liang, Z. Wang, K. Li, Y. Weng, Z. Lin, W. Fu, C. Che, Y. Che, Interstitial P-doped CdS with long-lived photogenerated electrons for photocatalytic water splitting without sacrificial agents, *Adv. Mater.* 30 (2018) 1705941, <https://doi.org/10.1002/adma.201705941>.
- [26] L. Zhang, R. Tong, S.E. Shirsath, Y. Yang, G. Dong, The crystalline/amorphous stacking structure of SnO<sub>2</sub> microspheres for excellent NO photocatalytic performance, *J. Mater. Chem. A* 9 (2021) 5000, <https://doi.org/10.1039/d0ta12101k>.
- [27] C. Wang, Y. Li, L. Huang, L. Yang, H. Wang, J. Liu, J. Liu, Z. Song, L. Huang, Enhanced photocatalytic antibacterial and degradation performance by n-p type 0D/2D SnO<sub>2-x</sub>/BiOI photocatalyst under LED light, *Chem. Eng. J.* 411 (2021), 128505, <https://doi.org/10.1016/j.cej.2021.128505>.
- [28] J. Wang, G. Li, Z. Li, C. Tang, Z. Feng, H. An, H. Liu, T. Liu, C. Li, A highly selective and stable ZnO-ZrO<sub>2</sub> solid solution catalyst for CO<sub>2</sub> hydrogenation to methanol, *Sci. Adv.* 3 (2017), e1701290, <https://doi.org/10.1126/sciadv.1701290>.
- [29] S. Das, K.G. Girija, A.K. Debnath, R.K. Vatsa, Enhanced NO<sub>2</sub> and SO<sub>2</sub> sensor response under ambient conditions by polyol synthesized Ni doped SnO<sub>2</sub> nanoparticles, *J. Alloy. Compd.* 854 (2021), 157276, <https://doi.org/10.1016/j.jallcom.2020.157276>.
- [30] L. Zhang, L. Li, Y. Cao, Y. Xiong, S. Wu, J. Sun, C. Tang, F. Gao, L. Dong, Promotional effect of doping SnO<sub>2</sub> into TiO<sub>2</sub> over a CeO<sub>2</sub>/TiO<sub>2</sub> catalyst for selective catalytic reduction of NO by NH<sub>3</sub>, *Catal. Sci. Technol.* 5 (2015) 2188–2196, <https://doi.org/10.1039/c4cy01412j>.
- [31] D. Toloman, O. Pana, M. Stefan, A. Popa, C. Leostean, S. Macavei, D. Silipas, I. Perhaita, M.D. Lazar, L. Barbu-Tudoran, Photocatalytic activity of SnO<sub>2</sub>-TiO<sub>2</sub> composite nanoparticles modified with PVP, *J. Colloid Interface Sci.* 542 (2019) 296–307, <https://doi.org/10.1016/j.jcis.2019.02.026>.
- [32] S. Tada, N. Ochiai, H. Kinoshita, M. Yoshida, N. Shimada, T. Joutsuka, M. Nishijima, T. Honma, N. Yamauchi, Y. Kobayashi, K. Iyoki, Active sites on Zn<sub>x</sub>Zr<sub>1-x</sub>O<sub>2-x</sub> solid solution catalysts for CO<sub>2</sub>-to-methanol hydrogenation, *ACS Catal.* 12 (2022) 7748–7759, <https://doi.org/10.1021/acscatal.2c01996>.
- [33] P. Chen, W. Cui, H. Wang, X. Dong, J. Li, Y. Sun, Y. Zhou, Y. Zhang, F. Dong, The importance of intermediates ring-opening in preventing photocatalyst deactivation during toluene decomposition, *Appl. Catal. B Environ.* 272 (2020), 118977, <https://doi.org/10.1016/j.apcatb.2020.118977>.
- [34] T.K. Dixit, S. Sharma, A.S.K. Sinha, Development of heterojunction in N-rGO supported bismuth ferrite photocatalyst for degradation of Rhodamine B, *Inorg. Chem. Commun.* 117 (2020), 107945, <https://doi.org/10.1016/j.inoche.107945>.
- [35] J. Jiang, J. Gao, T. Li, Y. Chen, Q. Wu, T. Xie, Y. Lin, S. Dong, Visible-light-driven photo-fenton reaction with alpha-Fe<sub>2</sub>O<sub>3</sub>/BiOI at near neutral pH: boosted photogenerated charge separation, optimum operating parameters and mechanism insight, *J. Colloid Interface Sci.* 554 (2019) 531–543, <https://doi.org/10.1016/j.jcis.2019.07.038>.
- [36] S. Pan, S. Yu, W. Zhang, H. Zhu, W. Lu, L. Jin, Low threshold amplified spontaneous emission from tin oxide quantum dots: a instantiation of dipole transition silence semiconductors, *Nanoscale* 5 (2013) 11561–11567, <https://doi.org/10.1039/c3nr03523a>.
- [37] L. Qi, Y. Yang, P. Zhang, Y. Le, C. Wang, T. Wu, Hierarchical flower-like BiOI<sub>1-x</sub>Br<sub>x</sub> solid solution spheres with enhanced visible-light photocatalytic activity, *Appl. Surf. Sci.* 467–468 (2019) 792–801, <https://doi.org/10.1016/j.apsusc.2018.10.184>.
- [38] H. Jia, W. He, B. Zhang, L. Yao, X. Yang, Z. Zheng, Facile synthesis of bismuth oxyhalide nanosheet films with distinct conduction type and photo-induced charge carrier behavior, *Appl. Surf. Sci.* 441 (2018) 832–840, <https://doi.org/10.1016/j.apsusc.2018.02.030>.
- [39] J. Guo, Y. Liu, Y. Hao, Y. Li, X. Wang, R. Liu, F. Li, Comparison of importance between separation efficiency and valence band position: the case of heterostructured Bi<sub>3</sub>O<sub>4</sub>Br/ $\alpha$ -Bi<sub>2</sub>O<sub>3</sub> photocatalysts, *Appl. Catal. B Environ.* 224 (2018) 841–853, <https://doi.org/10.1016/j.apcatb.2017.11.046>.
- [40] T. Wang, S. Liu, W. Mao, Y. Bai, K. Chiang, K. Shah, J. Paz-Ferreiro, Novel Bi<sub>2</sub>WO<sub>6</sub> loaded N-biochar composites with enhanced photocatalytic degradation of Rhodamine B and Cr(VI), *J. Hazard. Mater.* 389 (2020), 121827, <https://doi.org/10.1016/j.jhazmat.2019.121827>.
- [41] X. Zhang, L. Zhang, T. Xie, D. Wang, Low-temperature synthesis and high visible-light-induced photocatalytic activity of BiOI/TiO<sub>2</sub> heterostructures, *J. Phys. Chem. C* 113 (2009) 7371–7378, <https://doi.org/10.1021/jp900812d>.
- [42] J. Di, J. Xia, M. Ji, B. Wang, X. Li, Q. Zhang, Z. Chen, H. Li, Nitrogen-doped carbon quantum dots/BiOBr ultrathin nanosheets: in situ strong coupling and improved molecular oxygen activation ability under visible light irradiation, *ACS Sustain. Chem. Eng.* 4 (2015) 136–146, <https://doi.org/10.1021/acssuschemeng.5b00862>.
- [43] D. Xu, H. Feng, Y. Dong, Q. Wang, G. Zhang, L. Lv, Z. Ren, P. Wang, Enhanced molecular oxygen activation on (001) facets of Zn-doped BiOCl nanosheets for ciprofloxacin degradation, *Adv. Mater. Interfaces* 7 (2020) 2000548, <https://doi.org/10.1002/admi.202000548>.
- [44] J. Di, J. Xia, M. Ji, B. Wang, S. Yin, Y. Huang, Z. Chen, H. Li, New insight of Ag quantum dots with the improved molecular oxygen activation ability for photocatalytic applications, *Appl. Catal. B Environ.* 188 (2016) 376–387, <https://doi.org/10.1016/j.apcatb.2016.01.062>.
- [45] X. Dong, W. Cui, H. Wang, J. Li, Y. Sun, H. Wang, Y. Zhang, H. Huang, F. Dong, Promoting ring-opening efficiency for suppressing toxic intermediates during photocatalytic toluene degradation via surface oxygen vacancies, *Sci. Bull.* 64 (2019) 669–678, <https://doi.org/10.1016/j.scib.2019.04.020>.
- [46] L. Chen, P. Chen, H. Wang, W. Cui, J. Sheng, J. Li, Y. Zhang, Y. Zhou, F. Dong, Surface lattice oxygen activation on Sr<sub>2</sub>Sb<sub>2</sub>O<sub>7</sub> enhances the photocatalytic mineralization of toluene: from reactant activation, intermediate conversion to product desorption, *ACS Appl. Mater. Interfaces* 13 (2021) 5153–5164, <https://doi.org/10.1021/acsami.0c20996>.
- [47] L. Chen, G. Pan, T.C. Yang, T.W. Chung, C.M. Huang, In situ DRIFT and kinetic studies of photocatalytic degradation on benzene vapor with visiblelight-driven silver vanadates, *J. Hazard. Mater.* 178 (2010) 644–651, <https://doi.org/10.1016/j.jhazmat.2010.01.133>.
- [48] J. Li, X. Dong, G. Zhang, W. Cui, W. Cen, Z. Wu, S.C. Lee, F. Dong, Probing the ring-opening pathways for efficient photocatalytic toluene decomposition, *J. Mater. Chem. A* 175 (2019) 1–9, <https://doi.org/10.1039/c8ta11627j>.
- [49] H. Einaga, K. Mochiduki, Y. Teraoka, Photocatalytic oxidation processes for toluene oxidation over TiO<sub>2</sub> catalysts, *Catalysts* 3 (2013) 219–231, <https://doi.org/10.3390/catal3010219>.
- [50] X. Zou, C. Yuan, Y. Dong, H. Ge, J. Ke, Y. Cui, Lanthanum orthovanadate/bismuth oxybromide heterojunction for enhanced photocatalytic air purification and mechanism exploration, *Chem. Eng. J.* 379 (2020), 122380, <https://doi.org/10.1016/j.cej.2019.122380>.
- [51] M. Li, D. Li, Z. Zhang, C. Ji, S. Zhou, W. Guo, C. Zhao, F. Liu, F. Han, Study on the performance and mechanism of degradation of toluene with non-thermal plasmas synergized supported TiO<sub>2</sub>/ $\gamma$ -Al<sub>2</sub>O<sub>3</sub> catalyst, *J. Environ. Chem. Eng.* 9 (2021), 105529, <https://doi.org/10.1016/j.jece.2021.105529>.
- [52] Y. Zhang, C. Wu, Z. Wang, J. Ji, H. Wan, W. Zou, Q. Tong, J. Sun, L. Dong, Y. Chen, Enhanced low-temperature catalytic performance for toluene combustion of CeO<sub>2</sub>-supported Pt-Ir alloy catalysts, *Appl. Surf. Sci.* 580 (2022), 152278, <https://doi.org/10.1016/j.apsusc.2021.152278>.